Available online at www.sciencedirect.com
ScienceDirect
Trans. Nonferrous Met. Soc. China 29(2019) 200−212
Transactions of Nonferrous Metals Society of China
www.tnmsc.cn

Carbothermic reduction of chromite fluxed with aluminum spent potlining

Dawei YU[1,2], Dogan PAKTUNC[1]

1. CanmetMINING, Natural Resources Canada 555 Booth Street, Ottawa, Ontario K1A 0G1, Canada;
2. School of Metallurgy and Environment, Central South University, Changsha 410083, China

Received 26 February 2018; accepted 13 June 2018

Abstract: Aluminum spent potlining (SPL) was employed as both the fluxing agent and a source of carbonaceous reductant for the carbothermic reduction of chromite, aiming to allow effective separation of alloy from the slag component. The experimental results show that the carbonaceous component of the SPL is more reactive towards chromite reduction compared to graphite. The formation of refractory spinel ($MgAl_2O_4$) on chromite particles hinders further reduction and alloy growth. The slag-making components of the SPL (e.g. nepheline and NaF) form molten slags at low temperatures (~1300 °C) and partly dissolve the refractory spinel as well as the chromite. Destruction of the spinel layer with enhanced mass transfer greatly improves the alloy growth, which can be further promoted by reduction at a higher temperature (e.g. 1500 °C). Ferrochrome alloy particles grow large enough at 1500 °C in the presence of SPL, allowing effective separation from the slag component using elutriation separation.
Key words: chromite; carbothermic reduction; ferrochrome; aluminum spent potlining

1 Introduction

Ferrochromium alloy, as the essential virgin raw material for stainless steel production, is produced from carbothermic smelting reduction of chromite $(Mg,Fe)(Cr,Al,Fe)_2O_4$ in a submerged arc furnace (SAF). Slag-making fluxes such as quartzite, dolomite, or limestone [1] are used to react with the refractory components of the chromite (e.g. MgO, Al_2O_3) to produce a molten slag that separates from the molten ferrochromium alloy in the SAF. Due to the extremely endothermic nature of the carbothermic reduction reactions and high temperatures associated with the SAF operation, it is electric-energy-intensive, with the specific energy consumption (SEC) ranging from 2.4 to 4.8 MW·h/t of ferrochrome produced [2]. Pre-reduction of chromite before SAF could significantly reduce the SEC and the operation cost, because cheaper solid carbonaceous reductant such as fine anthracite, coke or char [3] could be used for partial reduction, and fossil fuels could be used for pre-heating the charge usually in a rotary kiln, which effectively reduce the subsequent electricity consumption by SAF [4,5].

Generally speaking, significant Fe reduction takes place prior to Cr reduction during the carbothermic chromite reduction [6−8]. Due to the presence of refractory component (i.e. MgO and Al_2O_3) in the chromite, a rim of secondary spinel ($MgAl_2O_4$) would form on the surface of chromite particles, inhibiting further reduction, especially Cr reduction [8−11].Various fluxes therefore have been studied in accelerating the carbothermic chromite reduction and metallization, such as silica (SiO_2) [7,11,12−15], lime (CaO) [16], $CaCO_3$ [17], borates [18], NaOH [19], flux mixtures containing at least three of the components CaO, SiO_2, Al_2O_3, MgO, CaF_2 [10], fluoride-containing mixtures such as CaF_2−NaF and fluorspar-feldspar-silica [11]. It was generally accepted that with the addition of silica flux, reduction was accelerated via dissolution of the refractory rim (i.e. $MgAl_2O_4$) or chromite [10,14−15]. Similar effect can be achieved with other fluxes.

In attempts to further reduce the SEC, we investigated the possibility of eliminating the use of SAF for ferrochrome production, by reducing the chromite at a lower temperature with the addition of $CaCl_2$ [20,21] and NaOH [19] as additives. In addition, we have tested spent potlining (SPL) as a special flux. Without the use of a SAF, it becomes critically important to promote the alloy growth during carbothermic reduction, because it allows feasible subsequent separation of ferrochrome alloys from the unwanted materials by grinding the product first for liberation followed by conventional separation techniques, such as gravity, density or

Corresponding author: Dawei YU; Tel: +86-731-88876255; E-mail: dawei.yu@csu.edu.cn
DOI: 10.1016/S1003-6326(18)64929-5

magnetic separations [20,21]. This is one of the objectives of the current study.

SPL is a waste material produced from aluminum smelters with a generation rate of about 22 kg/t of aluminum produced [22]. On a global scale, approximately one million tonnes of SPL is produced annually [23,24]. SPL is characteristic of its relatively high carbon (13%−69%, mass fraction) and fluorides content (7.5%−22%, mass fraction) [25], which draws much attention in its reutilization in other industries. Its composition varies, but the common major components are graphite, fluorides (e.g. NaF, Na_3AlF_6, CaF_2), and oxides (e.g. $NaAl_{11}O_{17}$, Al_2O_3, SiO_2) [22−23]. SPL can be used both as fuel/carbonaceous reductant and for decreasing the slag viscosity in the pig iron industry [26], ferroalloys industry [27], and in Ni/Cu smelters [28,29]. Because fluorides can improve slag formation in steel processing, SPL can be used to substitute for CaF_2 [22]. In addition to its application in the iron and steel industries [26,30,31], it has also been used in the mineral wool, and cement industries [32]. In this work, the carbon content (mainly as graphite) of the SPL can substitute for solid carbonaceous reductant for chromite reduction, while its fluorides and Na-compounds can be used as the fluxing agent to produce a molten slag of low melting point. The formation of low melting point slag could potentially promote the carbothermic chromite reduction and enhance the growth of ferrochrome alloys at lower temperatures, by dissolving the refractory $MgAl_2O_4$ layer forming on chromite particles and promoting the transfer of Fe and Cr as ionic species through the molten slag.

2 Experimental

2.1 Materials

The chromite ore from the Ring of Fire region of Ontario, Canada, was ground and sieved to 75−105 μm for the high-temperature experimental studies. Its chemical composition is provided in Table 1 with the mineralogical composition of the chromite in the ore being $(Mg_{0.5}Fe_{0.5})(Cr_{1.4}Fe_{0.1}Al_{0.5})O_4$. In addition to chromite, there are minor amounts of gangue minerals in the ore. These are clinochlore $(Mg,Fe)_5Al(Si_3Al)O_{10}(OH)_8$, magnesite ($MgCO_3$) and phlogopite $KMg_3(Si_3Al)O_{10}(OH)_2$.

Table 1 Composition of chromite ore of 75−105 μm fraction (mass fraction, %)

Cr_2O_3	FeO	MgO	Al_2O_3	SiO_2	TiO_2	V_2O_5	NiO	K_2O
44.4	19.7	14.1	10.8	4.5	0.3	0.2	0.2	0.2

The SPL obtained from an aluminum smelter was pulverized and sieved to produce three size fractions (i.e. 75−105 μm, 44−75 μm, and 25−44 μm). The SPL size fraction of 44−75 μm was used for experiments unless specified otherwise. Composition of the SPL is listed in Table 2. XRD analysis (Fig. 1) indicates the presence of graphite, nepheline ($NaAlSiO_4$), NaF, and $Na_2O(Al_2O_3)_{11}$ as the main crystalline phases. As seen, both the carbon and fluoride contents are in the lower range of those reported in the literature. Natural flake-shaped graphite powder (99.9995% pure) in the particle size range of 44−75 μm was used as the carbonaceous reductant, in addition to the graphite present in the SPL.

Table 2 Composition of SPL (mass fraction, %)

SiO_2	Al_2O_3	MgO	CaO	Na_2O	NaF	C
32.5	22.1	0.1	1.9	15.0	6.9	16.3

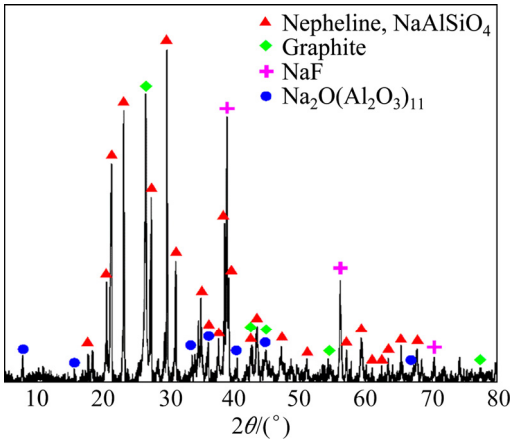

Fig. 1 XRD pattern of SPL used in this study, acquired using Cu K_α radiation

2.2 Electric furnace tests

A horizontal tube furnace (Radatherm Pty. Ltd) with six $MoSi_2$ heating elements and an alumina tube (inner diameter 63.5 mm) sealed with water-cooled flanges was used. The temperature was programmed prior to commencing the experiment. A sample containing 10 g chromite mixed with varying proportions of graphite and/or SPL was placed inside an alumina crucible (inner diameter 25 mm, depth 40 mm). With a constant Ar flow of 500 mL/min, the sample mixture was heated inside the horizontal tube furnace at a rate of 6.25 °C/min to a temperature in between 1300 and 1500 °C, and dwell for 2 or 3 h. The sample was rapidly cooled inside the furnace to room temperature before taking out for characterization. The average cooling rate was about 8 °C/min at temperatures above 500 °C. The offgas was analyzed continuously with a gas analyzer (ABB EL3020) for its CO and CO_2 concentrations throughout the test.

2.3 Separation of ferrochrome alloys from slag

The reduced product of about 8 g was firstly

crushed and ground in a mortar and pestle to allow 100% passing through the 150-mesh sieve (opening 106 μm), to allow effective liberation of the ferrochrome alloy particles from the unwanted slag component. The sample powder was further sieved to produce three size fractions (i.e. 63−106 μm, 37−63 μm, and <37 μm). Each size fraction was individually subjected to gravity separation using an elutriation tube, same as reported by FROST [33], by taking advantage of the density difference between the ferrochrome alloy and the unwanted slag particles in a counter current flow. Three products were obtained from each size fraction, namely concentrate, middling, and tailing. The concentrate is the portion rich in ferrochrome alloy, while the tailing is mainly composed of light slag particles. The middling portion contains both alloy and slag particles, requiring further separation.

2.4 Analytical methods

One-inch polished sections were prepared from sample products which were subjected to analysis by scanning electron microscopy (SEM, Hitachi S-3200N) coupled with an energy dispersive spectrometer (Quantax EDS, Bruker), using an accelerating voltage of 20 kV. For the analysis of particle size distribution of the alloy particles in the reduced product, SEM images were taken at the magnification of 50, covering all surface area of the polished section. All SEM images were subsequently analyzed by the image analysis software ImageJ [34] for the particle size distribution of alloy particles. For the estimation of the diameter of each alloy particle from its measured surface area, the assumption was made that the alloy particles are spherical, admitting that they are irregular in shape to various degrees.

Chemical composition of the solid product was analyzed by firstly digesting it into a mixture of nitric and phosphoric acid solution at temperatures higher than 200 °C under high pressure in a microwave reaction system (Anton Paar Multiwave PRO), followed by analyzing the aqueous solution using inductively coupled plasma atomic emission spectrometry (ICP-AES, Varian VISTA RL). For qualitative phase identification, samples were also analyzed by X-ray powder diffraction (XRD, Rigaku D/MAX 2500) with Cu K_α radiation at 40 kV, 200 mA.

3 Results and discussion

3.1 Thermodynamic considerations and mechanisms of alloy growth

As stated, dissolution of refractory spinel ($MgAl_2O_4$) into the molten slag phase is critically important in further promoting the later stage of chromite reduction. Its extent of dissolution can be influenced by many factors, such as the slag composition and volume, temperature and residence time [9]. The influence of temperature and slag composition was firstly evaluated using the Equilib module of the thermochemical software FactSage [35]. As indicated by Table 2 and Fig. 1, nepheline and NaF are the main slag-making components of the SPL used in the work. Therefore, thermodynamic calculations were conducted by equilibrating $MgAl_2O_4$ with an equal mass of the (nepheline+NaF) mixture at various temperatures in the range of 1200−1700 °C (Fig. 2). The mass ratio of nepheline/(nepheline+NaF) ranged from 0 to 1, to reflect the variability in the slag/SPL composition. As seen, no molten slag formed at temperatures below 1300 °C. However, reactions between $MgAl_2O_4$ and the SPL component can take place at these low temperatures, forming new phases of $NaMgF_3$ and $NaAlO_2$, indicated by FactSage calculation [35]. This resulted in the residual spinel of only 30 wt% at the nepheline/(nepheline+NaF) ratio of 0.4 g/g, as shown in Fig. 2(a). Formation of molten slag takes place at temperatures higher than 1300 °C. In general, higher temperature resulted in the dissolution of

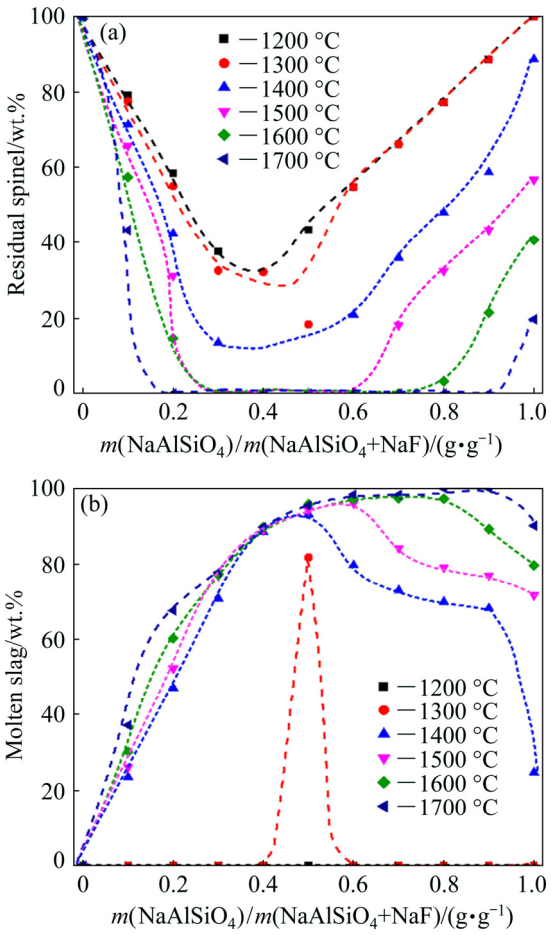

Fig. 2 Amounts of residual spinel ($MgAl_2O_4$) (a), and molten slag formed (wt.% of total mass) (b), after equilibrating $MgAl_2O_4$ with equal mass of ($NaAlSiO_4$ + NaF) mixtures at various temperatures

higher amounts of $MgAl_2O_4$, and the optimum ratio of nepheline/(nepheline+NaF) in the SPL to achieve the highest molten slag formation and dissolution of $MgAl_2O_4$ is at approximately 0.5 g/g. The SPL used in this work has a nepheline/(nepheline+NaF) ratio of approximately 0.9 g/g.

Growth of an existing alloy particle can be attributed to a combination of mainly two mechanisms: (1) continuous reduction reactions taking place on the surfaces of the alloy/carbon particles, resulting in metallization and alloy growth, and (2) coalescence of adjacent alloy particles further increasing the alloy particle sizes. The second mechanism can be greatly promoted by employing a higher temperature, slag of a lower melting point and lower viscosity, and introducing turbulence to the melt. Viscosity of the reduction system in the presence of both solid (e.g. $MgAl_2O_4$, chromite) and melt (e.g. molten slag) can be described by the Einstein-Roscoe equation (Eq. (1)) [36,37], in which η_r is the relative viscosity, η is the viscosity of the crystal+melt system, η_m is the melt viscosity, ϕ is crystallinity, and σ is a constant (e.g. 0.6 as reported by MARSH [38]). Na-bearing components and fluorides in the SPL are known to be effective in decreasing the molten slag viscosity (η_m) [28]. Crystallinity (ϕ) can be decreased by reducing the amounts of residual spinel and promoting the molten slag formation, which could be realized by increasing temperature and with SPL addition (Fig. 2). Mobility of the alloy particles in the material bed during carbothermic chromite reduction can be improved by creating turbulence in the partial-melt system of relatively low viscosity, via natural convection of the melt and/or formation of CO and CO_2 gas bubbles in the melt from reduction reactions. Highly mobile alloy particles have higher chance of colliding/contacting with each other, which is a prerequisite for the coalescence of alloy particles. The probability of successful alloy coalescence upon collision/contact can be promoted if the alloy particles become completely molten. Figure 3 exhibits the liquidus projection of the Cr−Fe−C system, plotted using FactSage [35]. As seen, the liquidus temperature of the Cr−Fe−C alloy increases with the increasing concentration of Cr and varies significantly with the C concentration. Ferrochrome carbide of $(Cr,Fe)_7C_3$, or simply M_7C_3, is generally the primary carbide phase in the high-carbon ferrochrome [39,40]. Based on this figure, a temperature of higher than 1400 °C is required to completely melt the alloy at a Cr/Fe mass ratio of approximately 2:1, which is based on the Cr/Fe ratio of the starting chromite ore (Table 1).

$$\eta_r=\eta/\eta_m=(1-\phi/\sigma)^{-2.5} \quad (1)$$

3.2 Influence of SPL particle size

The influence of SPL addition (45 wt.% of ore) with the variation of SPL particle size was evaluated (Fig. 4). The reactivity of the carbonaceous component of the SPL (i.e. graphite) towards chromite reduction can be reflected by the CO evolution in Fig. 4, because no extra graphite was added in these tests. The evolution of CO_2 at 80 min (or about 600 °C) was due to the thermal decomposition of magnesite ($MgCO_3$), which is present as a gangue mineral in the chromite ore [8]. Reduction of chromite initiated at about 120 min (or 900 °C), indicated by the generation of CO gas. A higher reduction rate was achieved with a smaller SPL particle size range, due to the higher surface area of graphite particles available for reduction. Termination of the reduction reactions was due to the complete consumption of the graphite present in the sample, because the amount of graphite in the SPL was far from the stoichiometric amount required for complete chromite reduction. Assuming the formation of CO and M_7C_3 type carbide as the reduction products, the chromite ore requires stoichiometric amount of approximately 18.5 wt.% C for complete reduction.

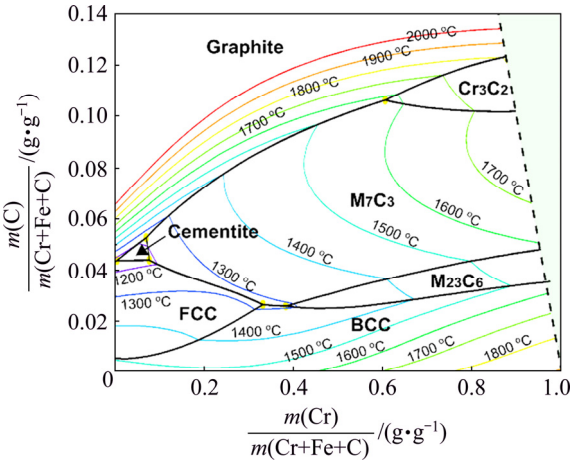

Fig. 3 Liquid projection of Cr−Fe−C system, plotted using FactSage [35]

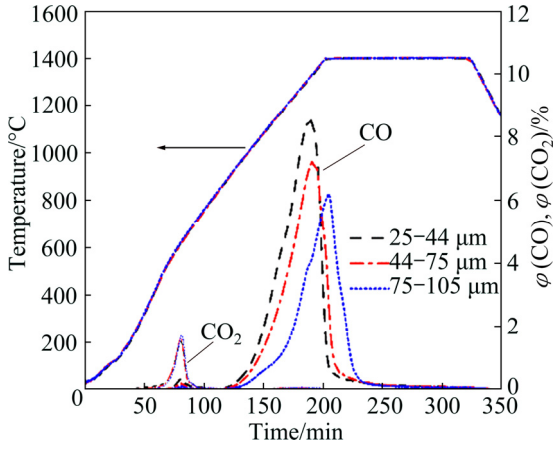

Fig. 4 Temperature and offgas CO and CO_2 profiles for tests with addition of SPL of varying particle sizes, in the absence of graphite addition

Figure 5 exhibits the cross section of the product with the addition of 25−44 μm SPL. Partial reduction of chromite by the carbonaceous component of SPL resulted in the formation of relatively large ferrochrome alloy particles (Fig. 5(a)). With enhanced contrast, Fig. 5(b) shows the presence of both elongated and equiaxed M_7C_3 crystals (grey), embedded in a matrix of Fe-rich alloy (white). Based on the EDS analysis, the M_7C_3 crystals have an average Cr:Fe mass ratio of 2.26:1, while it was only 0.16:1 for the Fe-rich alloy. The Fe-rich alloy containing about 2.9 wt.% C is a metastable eutectic, according to LEŠKO and NAVARA [40], who also demonstrated that this particular microstructure is characteristic of a rapidly-cooled ferrochromium. As seen in Figs. 5(a) and (c), partially reduced chromite (PRC) occurred as disseminated particles in the slag matrix (mainly nepheline based on XRD analysis) which was apparently molten at 1400 °C. Partial reduction of chromite also produced the stripe-shaped Fe-rich ferrochrome alloy within the PRC particles. Surface roughness and cracks on the PRC particles were due to the dissolution of chromite/spinel into the molten slag, with the dissolved ionic Cr and Fe species being transported and reduced on the graphite/alloy particles. Continued dissolution of the chromite/spinel by the molten slag also resulted in the precipitation of the secondary spinel particles that formed at the bottom of the crucible as a thin layer (Fig. 5(d)). The coalescence of ferrochrome alloy into large particles (Fig. 5(a)) suggests relatively low viscosity for the molten slag, and the presence of turbulence in the melt, possibly resulting from the evolution of CO/CO_2 gas bubbles from reduction reactions.

3.3 Influence of temperature

Chromite was reduced in the presence of both

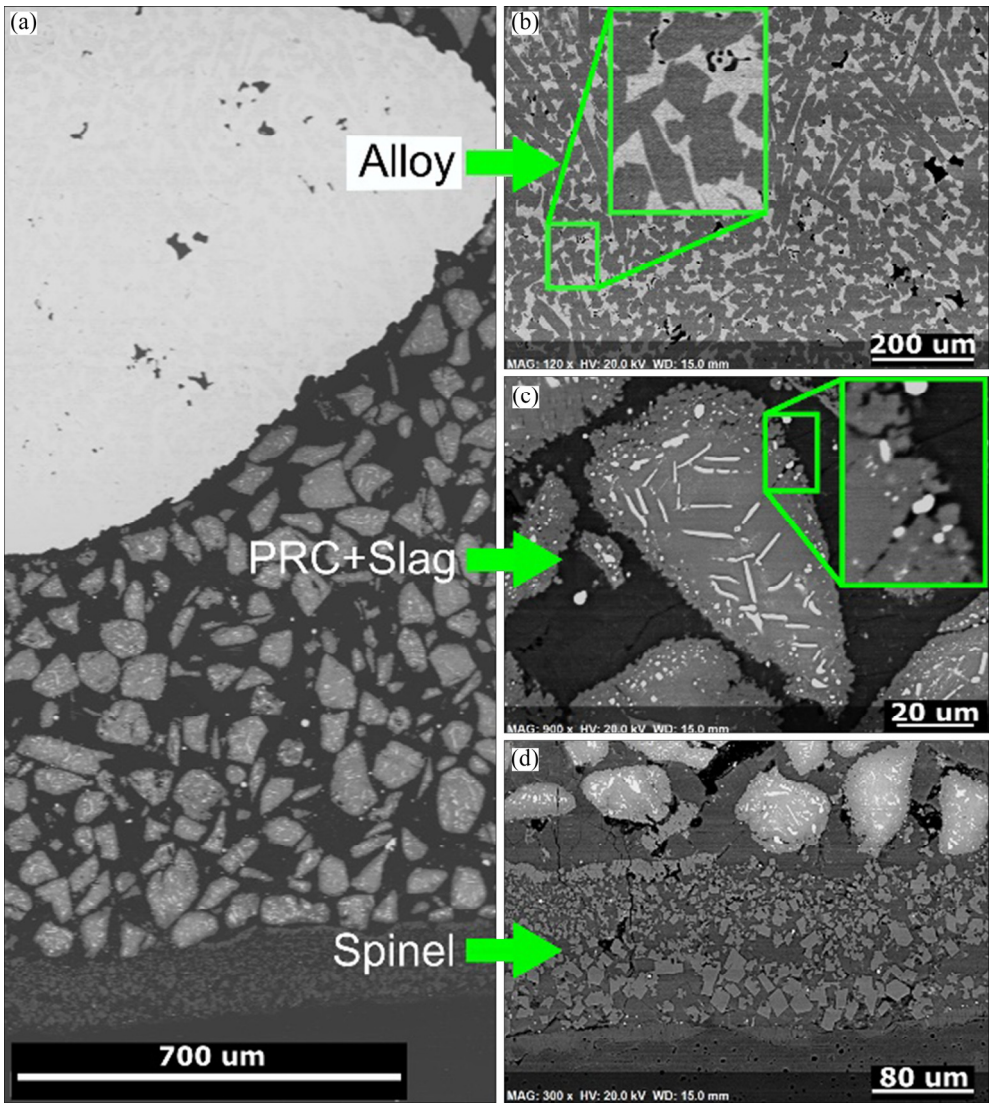

Fig. 5 Cross section (a) of product with addition of 25−44 μm SPL, revealing formation of alloy particle (diameter ~2.6 mm) (b), partially reduced chromite (PRC) suspended in slag (c), and secondary spinel particles re-crystallized in molten slag as layer measuring about 110 μm in thickness at bottom of crucible (d)

graphite (15 wt.% of ore) and SPL (45 wt.% of ore) at temperatures of 1300, 1400 and 1500 °C (Fig. 6). Similar to Fig. 4, thermal decomposition of magnesite took place at about 600 °C, leading to the evoluation of CO_2. Evolution of CO gas was from the carbothermic reduction of chromite. A higher degree of reduction can be achieved at a higher reduction temperature, as indicated by the relative intensity of the CO peaks in Fig. 6. Two reduction stages are observed for each test. Carbothermic reduction in the first stage was relatively fast, represented by the strong CO peak. Preferential reduction of Fe species could have taken place in this early reduction stage [5−8, 41]. For the tests at 1300 and 1400 °C, a much slower reduction rate was observed at the second reduction stage, compared to that of the first stage. This slower later stage of reduction was suggested to be partly resulting from the formation of a refractory oxide layer on the chromite particles, which hindered the outward transfer of reducible ions of Cr and Fe from chromite cores [8]. It is also suggested that predominent reduction of Cr species took place in this later stage [5−8,41]. In contrast, a secondary intensive CO peak appeared during the second stage of reduction at 1500 °C. The CO concentration decreased quickly to near zero after 270 min (Fig. 6), or 45 min after reaching the isothermal temperature of 1500 °C, indicating a near complete reduction of chromite has taken place.

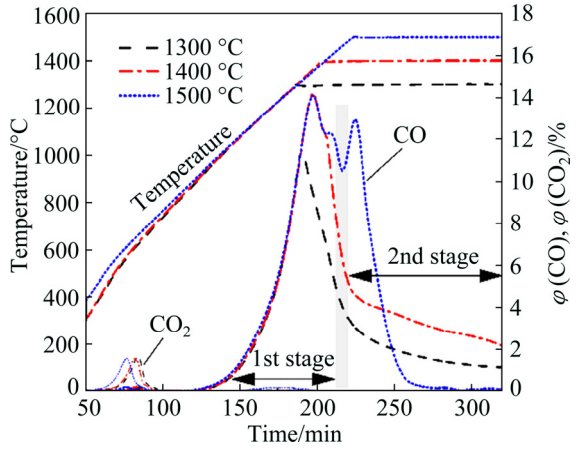

Fig. 6 Temperature and offgas CO and CO_2 profiles for tests with variation of reduction temperature

Results from the XRD and SEM analyses of the products are given in Figs. 7 and 8, respectively. Because of a much lower degree of reduction at 1300 °C, its XRD pattern shows the presence of both unreacted graphite and chromite in the product. Phases of carbide (M_7C_3), ferrochrome alloys (CrFe), and refractory spinel ($MgAl_2O_4$) are identified by XRD as the reduced products at all temperatures. Morphology of the reduced product at 1300 °C (Figs. 8(a) and (b)) revealed that the PRC particles were disseminated in the slag matrix which appeared to be molten at 1300 °C. Very limited degree of reduction at this low temperature resulted in the formation of small alloy particles, mostly on the surface of the molten slag (Fig. 8(a)). The particle size and shape of the alloys resembled that of the starting flake-shaped graphite powders, indicating that metallization took place mostly on the graphite particles. It also suggests that the alloy particles were not completely molten at 1300 °C, because they would lose their original shapes and become somewhat spherical, driven by the minimization of the surface energy of molten alloys, as appeared at 1400 and 1500 °C (Figs. 8(c), (e)). This is in good agreement with the liquid projection of the Cr−Fe−C system as shown in Fig. 3. The presence of a refractory spinel ($MgAl_2O_4$) layer was observed on the PRC particles at both 1300 and 1400 °C, as shown in Figs. 8(b) and (d), respectively. The formation of this refractory oxide layer on chromite particles greatly limited the rate of reduction, resulting in the slower second reduction stage (Fig. 6).

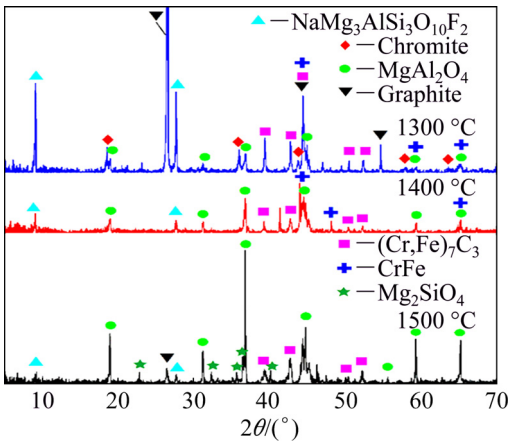

Fig. 7 XRD patterns of products at various reduction temperatures

Figure 9 exhibits the elemental mapping of the PRC particles embedded in the slag matrix produced from 1400 °C. The Al and Mg distributions further demonstrate the presence of a spinel layer on the PRC particles. Monoxide (MgO) is also observed beneath the spinel layer in localized areas. In addition, sheet-shaped Mg-bearing silicate crystals have formed in the silicate slag as shown in the Mg mapping, which was identified by XRD (Fig. 7) as a type of mica ($NaMg_3AlSi_3O_{10}F_2$). Formation of Mg-bearing mica in the slag matrix was due to the partial dissolution of spinel/chromite into the slag-making components of the SPL, because the starting SPL contains little Mg. This is in good agreement with the thermodynamic prediction as shown in Fig. 2. Comparatively, near-complete reduction has taken place at a higher temperature of 1500 °C, reflected by the disappappearance of the PRC particles (Fig. 8(e)).

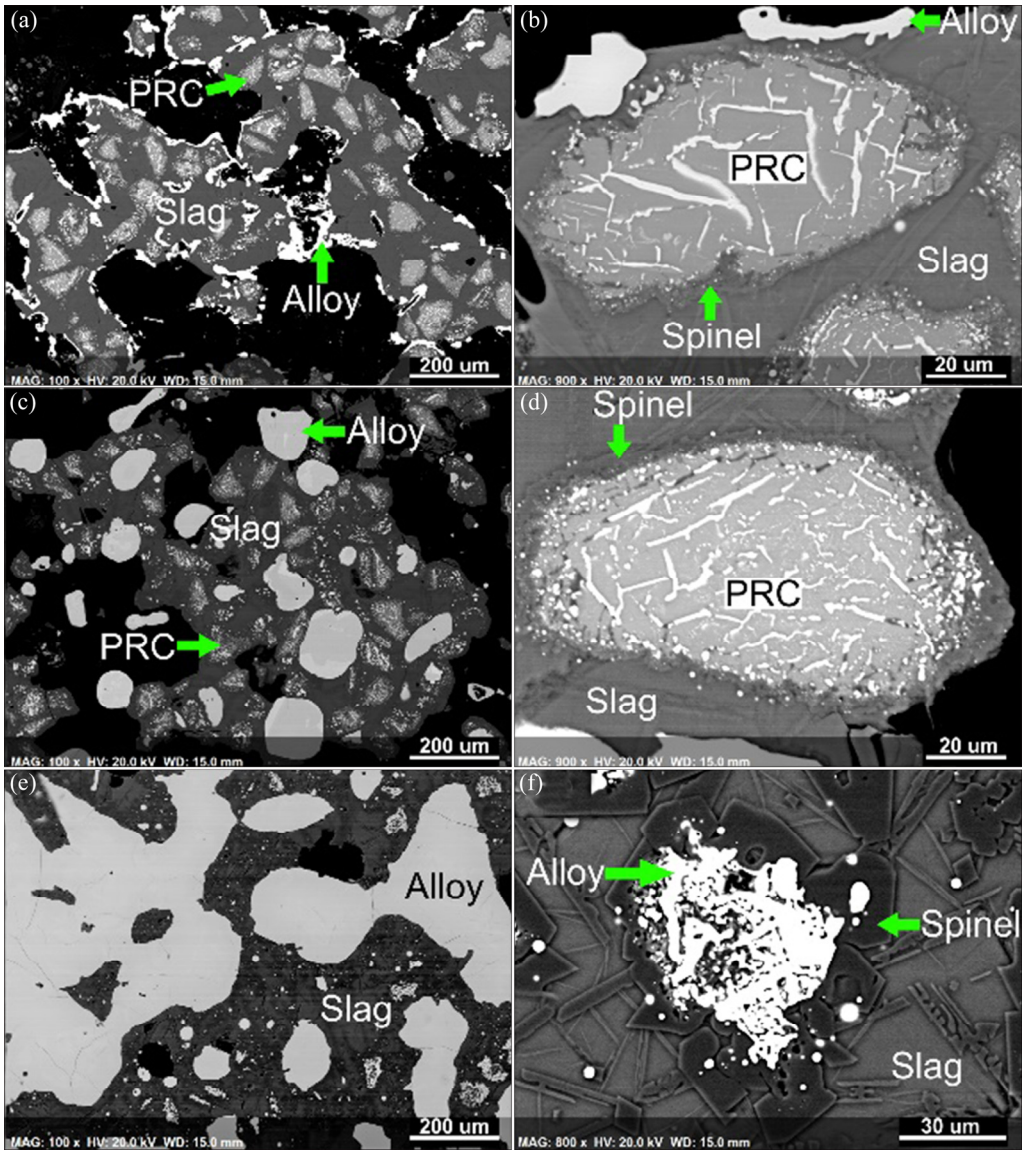

Fig. 8 Cross sections of products at different reduction temperatures of 1300 °C (a,b), 1400 °C (c,d), and 1500 °C (e,f)

Coalescence of the alloy particles at this temperature resulted in significant alloy growth, which was likely caused partly by the higher solubility of spinel into the molten slag, removing the refractory physical barriers. Dissolution of spinel into the molten slag is evidenced by the presence of both the mica and Mg_2SiO_4 based on XRD analysis (Fig. 7). Figure 8(f) exhibits an un-coalesced small alloy particle surrounded by the solid spinel layer, demonstrating that the spinel layer acted as a physical barrier which prevented the enclosed alloy particle from coalescing with other alloy particles.

SPL-assisted chromite reduction involved formation of molten slag phases especially at higher temperatures. This might impact negatively on the reduction process if it is applied in a rotary kiln due to its possible operational issues resulting from the formation of excessive dam-ring [42]. Therefore, equipment that is not so susceptible to dam-ring formation should be investigated for its potential implementation on an industrial scale.

3.4 Influence of SPL amount

In order to further investigate the influence of SPL addition on chromite reduction, varying combinations of graphite and SPL addition were employed, i.e. 22 wt.% graphite (22C), 45 wt.% SPL (45SPL), 15 wt.% graphite + 20 wt.% SPL (15C20SPL), and 15 wt.% graphite + 45 wt.% SPL (15C45SPL), as shown in Fig. 10. As seen, reduction started at about 168 min (or 1200 °C) in the absence of SPL, indicated by its CO concentration profile. In comparison, carbothermic reduction of chromite initiated at about 130 min (or 960 °C) in the presence of SPL, which is about 240 °C lower. This demonstrates the higher reactivity of the carbonaceous component of the SPL for carbothermic reduction,

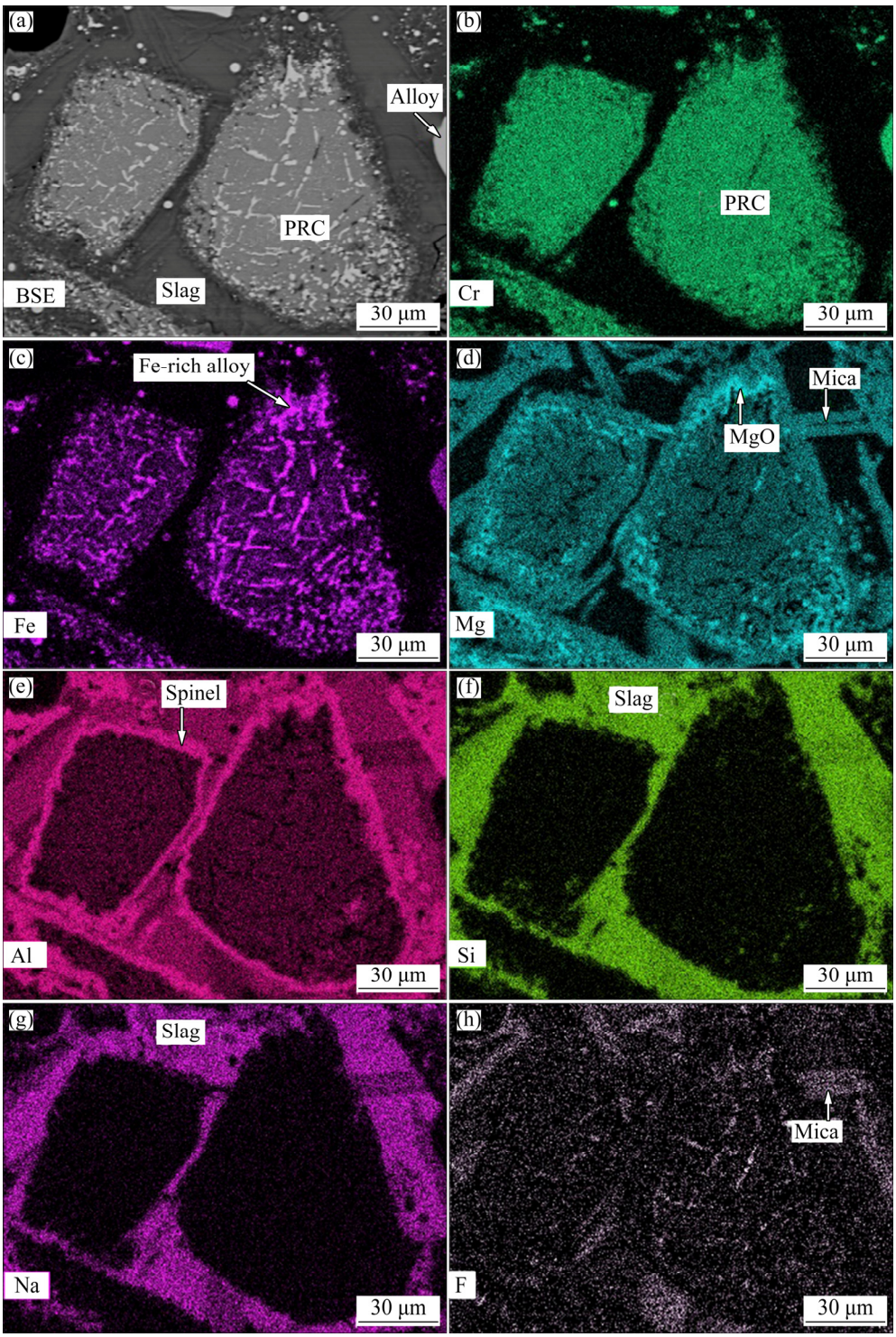

Fig. 9 Elemental mapping of PRC particles embedded in slag matrix, produced at 1400 °C

especially at low reduction temperatures. Because of the insufficient amount of carbon required for complete reduction in both the tests of 45SPL and 15C20SPL, reduction terminated at an early stage due to the complete consumption of carbon. Compared to the test 22C, a higher reduction rate is observed for the test 15C45SPL at the later stage (i.e. after 250 min in Fig. 10). This is due to the enhancement of the carbothermic chromite reduction by the partial dissolution of the refractory spinel layer in the presence of SPL. Figure 11 exhibits the cross sections of the product from the tests 22C (a) and 15C20SPL (b). PRC particles are observed in both samples with a layer of spinel, indicating an incomplete reduction of chromite. Monoxide (MgO) formed beneath the spinel layer in the absence of SPL (Fig. 11(a)), with its presence also confirmed by XRD

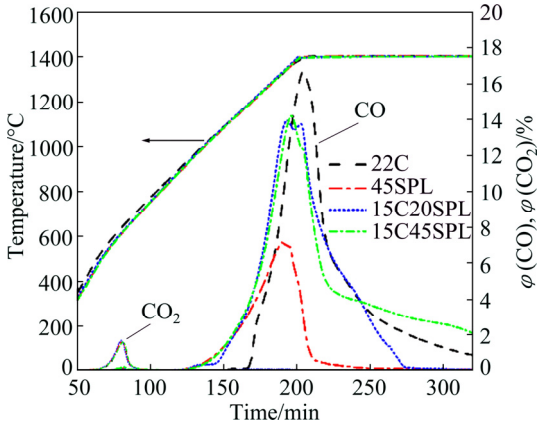

Fig. 10 Temperature profiles and offgas CO and CO_2 concentrations for chromite reduction with 22 wt.% graphite (22C), 45 wt.% SPL (45SPL), 15 wt.% graphite+20 wt.% SPL (15C20SPL), and 15 wt.% graphite+45 wt.% SPL (15C45SPL)

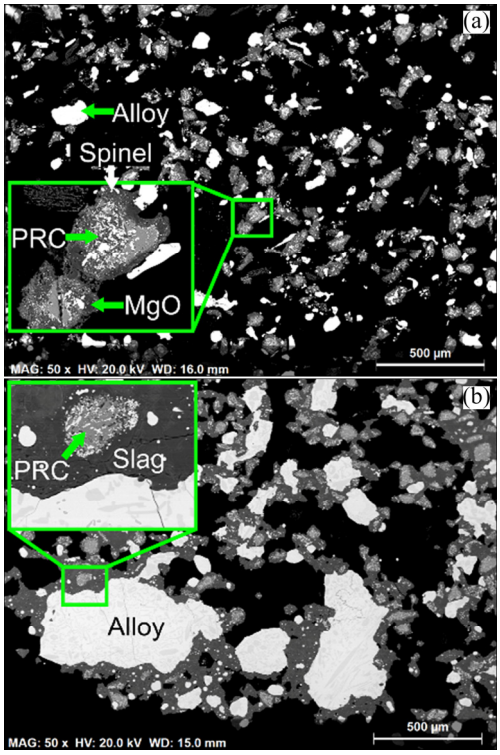

Fig. 11 Cross sections of products from chromite reduction with 22 wt.% graphite (a), and 15 wt.% graphite + 20 wt.% SPL (b)

analysis (Fig. 12). Assuming M_7C_3 as the alloy product, the carbothermic reduction of chromite can be represented by Eq. (2), based on the average composition of the chromite phase used in the study. As shown in this reaction equation, formation of this secondary refractory phase MgO was due to the lower Mg:Al molar ratio in the $MgAl_2O_4$ (i.e. 0.5:1) compared to that of the pristine chromite (i.e. 1.0:1).

$$7(Mg_{0.5}Fe_{0.5})(Cr_{1.4}Fe_{0.1}Al_{0.5})O_4+25.25C= 2Cr_{4.9}Fe_{2.1}C_3+1.75MgAl_2O_4+1.75MgO+19.25CO \quad (2)$$

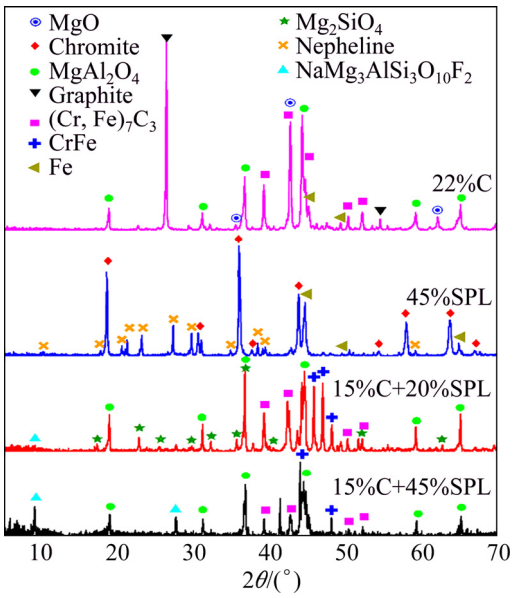

Fig. 12 XRD patterns of products from chromite reduction with varying combinations of graphite and SPL

As illustrated in Fig. 11, the addition of SPL significantly increased the alloy particle sizes. In order to allow a quantitative comparison, selected alloy particle size distributions from four tests are shown in Fig. 13. As seen, 50 vol.% of the alloys are smaller than 30 μm ($D50$) in the absence of SPL, and 100 vol.% are below 80 μm. $D50$ increased to 67 and 101 μm in the presence of 45% and 20 wt.% SPL, respectively, due to the alloy growth mechanisms which was discussed in Section 3.1. The fact that the alloy particle size distribution of the test 15C20SPL is higher than that of 15C45SPL is likely due to the following factors. Generally speaking, significant Fe reduction took place before Cr reduction [6−8]. Due to the lower degree of reduction/metallization for the test 15C20SPL compared to 15C45SPL (Fig. 10), the alloy particles of 15C20SPL are therefore generally Fe-richer

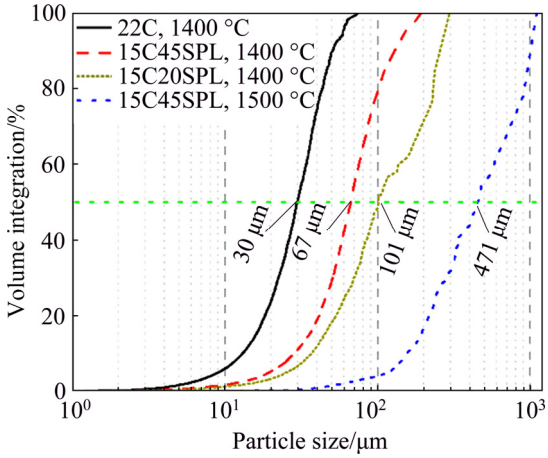

Fig. 13 Volume integration of alloy particles as function of alloy particle size

compared to that of 15C45SPL, exibiting lower melting temperatures (Fig. 3). Alloy particles of lower melting temperatures (i.e. lower Cr:Fe mass ratio) have higher tendency of coalescence upon collision/contact, resulting in larger particle sizes. It is also seen from Fig. 13 that increasing the reduction temperature to 1500 °C is most effective in further increasing the alloy particle sizes in the presence of SPL ($D50$=471 μm), due mainly to the higher solubility of refractory spinel into the molten slag as well as the enhanced coalesence of molten alloy particles at a higher temperature.

Based on EDS analysis, Fig. 14 exhibits the composition of alloy particles produced from the test 15C20SPL in relation to their particle sizes. These alloy particles contain two main phases, i.e. Cr-rich M_7C_3, and Si-bearing metastable eutectic phase (see Table in Fig. 14(a)). Based on the compositional change and their particle sizes, alloy particles can be classified into small, medium and large particles. Small particles (<20 μm) exhibit round shape in Fig. 14(a), and has a low Cr:Fe mass ratio of approximately 1.4:1, indicating that they formed during the early reduction stage and stopped growing. Medium particles (20−60 μm) has the highest Cr:Fe mass ratio of 2.4:1, suggesting that they evolved continuously till the late stage of reduction, but did not have much chance of coalescing with other alloy particles. Large alloy particles (>60 μm) were produced from significant alloy coalescence, with an average Cr:Fe mass ratio of 2.1.

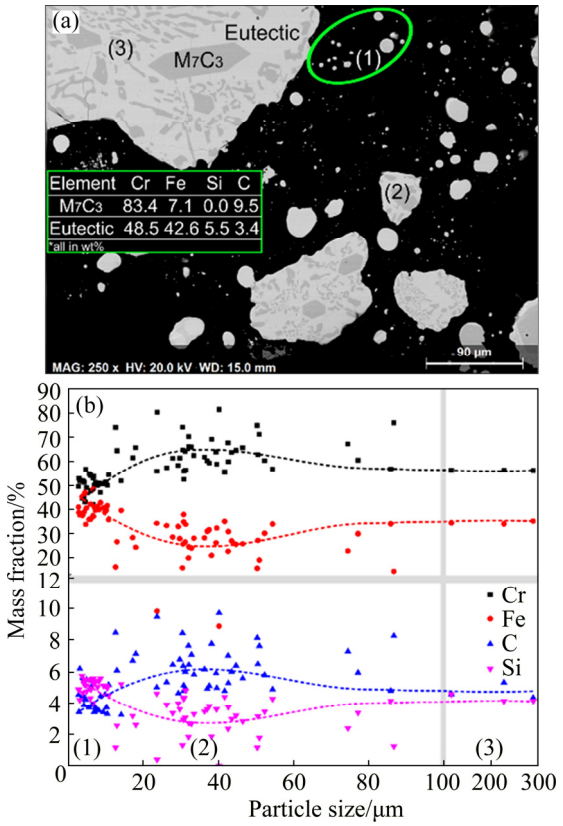

Fig. 14 Cross section of alloy particles from test 15C20SPL (a), and composition of individual alloy particles in relation to their respective particle sizes (b) (Alloy particles are categorized into (1) small, <20 μm; (2) medium, 20−60 μm; and (3) large, >60 μm, based on their sizes)

3.5 Elutriation separation

The product from chromite reduction with the addition of 15 wt.% graphite and 45 wt.% SPL at 1500 °C was subjected to sieving followed by elutriation separation for upgrading the alloy particles into a concentrate. As seen from Table 3, each particle size fraction was subjected to elutriation separation to produce three fractions, i.e. concentrate, middling, and tailings. SEM micrographs of the three size fractions before elutriation are shown in Figs. 15(a−c). As seen, alloy particles in all three size fractions were generally well liberated, and were present mostly as individual particles that were not associated with the slag component. Figures 15(d−f) exhibit the concentrate, middling and tailings fractions produced from elutriation separation of the 63−106 μm size fraction, which indicates that only a few slag particles were present in the concentrate fraction, and a few alloy particles were in the tailings fraction. This demonstrates the effectiveness of elutriation for upgrading the alloys into the concentrate. The combined concentrate from the three size fractions accounted for 37.0 wt.% of the total mass, while the combined tailing represents 56.9 wt.% (Table 3). The middling (6.1 wt.%) requires further processing for separation. Based on chemical analysis, Fig. 16 illustrates the elemental distribution of Cr, Fe, Mg, Al and Si among the combined concentrate, middling and tailing fractions. As seen, the recoveries of Cr and Fe into the combined concentrate fraction were 68.4 wt.% for both, and approximately 25 wt.% was lost in the form of alloys into the tailing fraction. The alloys in the tailing fraction was present as both liberated individual alloy particles and smaller alloy particles that were locked in the slag particles (Fig. 15(f)). Most Mg, Al and Si (89.4%, 88.8% and 74.0%, respectively, mass fraction) were rejected into the tailings fraction. It should also be noted that Si in the concentrate fraction

Table 3 Mass quantities of products from elutriation separation of three size fractions

Size fraction/μm	w(Concentrate)/%	w(Middling)/%	w(Tailing)/%	w(Total)/%
63−106	24.7	4.3	17.9	46.9
37−63	7.4	1.8	8.7	17.9
<37	4.9	0	30.3	35.2
Total	37.0	6.1	56.9	100

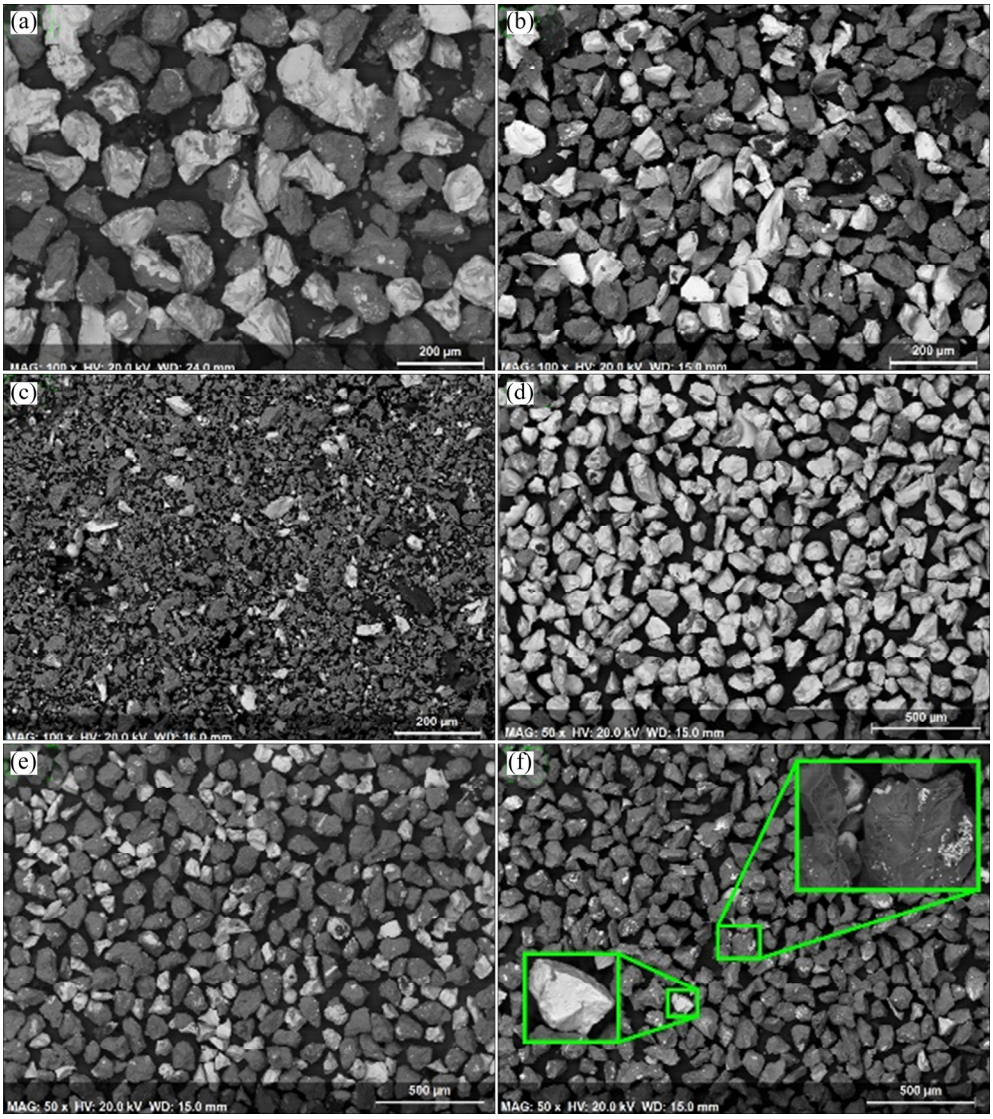

Fig. 15 SEM images of size fractions (63−106 μm (a), 37−63 μm (b), and <37 μm (c)), of reduced product before elutriation separations and concentrate (d), middling (e), and tailing (f) produced from elutriation separation of 63−106 μm size fraction (a) (White or light gray particles are alloys and dark gray particles are slag/gangue)

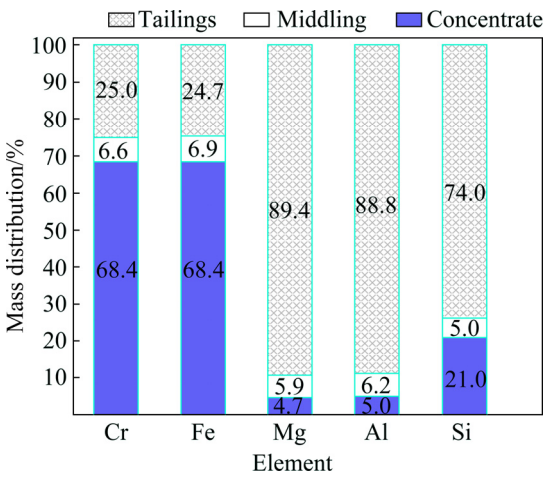

Fig. 16 Distribution of elements among concentrate, middling, and tailings

(21 wt.%) presented as both the siliceous slag and the Si-bearing alloy components, unlike Mg and Al which can only be found in the slag component. The combined concentrate fraction contained 53.0 wt.% Cr, 28.5 wt.% Fe, 4.8 wt.% Si, 1.4 wt.% MgO, and 2.8 wt.% Al_2O_3, based on chemical analysis.

4 Conclusions

(1) Experimental results show that the carbonaceous component of the SPL appeared to be more effective in reducing chromite compared to graphite, because it can reduce the starting temperature for chromite reduction by about 240 °C.

(2) The formation and growth of the refractory spinel ($MgAl_2O_4$) layer on the surface of each chromite

particle significantly hindered the chromite reduction and acted as a barrier for alloy growth. The main slag-making components of the SPL used were nepheline (Na_3AlF_6) and NaF, which were capable of forming low melting temperature slags and dissolving partly the refractory spinel layer, thereby promoting not only the carbothermic chromite reduction rate, but also the alloy growth.

(3) Because Fe-rich ferrochrome particles have a lower melting temperature, they exhibited a higher tendency of forming larger alloy particles because of the higher probability of coalescence upon collision/contact among alloy particles.

(4) Reduction at a higher temperature (e.g. 1500 °C) was more effective in promoting the alloy growth, by further promoting the dissolution of spinel into the molten slag, and by enhancing the coalescence of molten alloy particles.

(5) Formation of molten slags and alloys might impact negatively if it is applied in a rotary kiln due to potential dam-ring formation.

(6) Elutriation separation of the product from chromite reduction at 1500 °C in the presence of SPL demonstrated its effectiveness in upgrading the ferrochrome alloy particles into a concentrate containing 53.0 wt.% Cr and 28.5 wt.% Fe, with a 68.4 wt.% recovery of Cr and Fe, while most slag components were effectively rejected.

Acknowledgements

The following contributions are acknowledged: Shudip Faiyaz for performing the SEM analyses and the elutriation separation, Derek Smith for XRD analyses, Ruiping Wang for chemical analysis of the products, and KWG Resources Inc. for providing the chromite ore samples. The study was funded by NRCan under the Rare Earth Elements and Chromite R&D Program.

References

[1] BASSON J, DAAVITTILA J. Handbook of ferroalloys: Theory and technology [M]. New York: Butterworth-Heinemann Elsevier, 2013.

[2] JOHNSON J, RECK B K, WANG T, GRAEDEL T E. The energy benefit of stainless steel recycling [J]. Energy Policy, 2008, 36: 181−192.

[3] KLEYNHANS E L J, BEUKES J P, VAN ZYL P G, BUNT R J, NKOSI N S B, VENTER M. The effect of carbonaceous reductant selection on chromite pre-reduction [J]. Metallurgical and Materials Transactions B, 2017, 48: 827−840.

[4] CHAKRABORTY D, RANGANATHAN S, SINHA S N. Investigations on the carbothermic reduction of chromite ores [J]. Metallurgical and Materials Transactions B, 2005, 36B: 437−444.

[5] NAFZIGER R H, TRESS J E, PAIGE J I. Carbothermic reduction of domestic chromites [J]. Metallurgical Transactions B, 1979, 10B: 5−14.

[6] WANG Y, WANG L, XU J, CHOU K C. Kinetics of carbothermic reduction of synthetic chromite [J]. Journal of Mining and Metallurgy, Section B: Metallurgy, 2014, 50: 15−21.

[7] WEBER P, ERIC R H. The reduction mechanism of chromite in the presence of a silica flux [J]. Metallurgical Transactions B, 1992, 24: 987−995.

[8] YU D, PAKTUNC D. Kinetics and mechanisms of the carbothermic reduction of chromite in the presence of nickel [J]. Journal of Thermal Analysis and Calorimetry, 2018, 132: 143−154.

[9] HAYES P C. Aspects of SAF smelting of ferrochrome [C]//Tenth International Ferroalloys Congress. Cape Town, South Africa: South African Institute of Mining and Metallurgy, 2004: 1−14.

[10] NEUSCHUTZ D, JANBEN P, FRIEDRICH G, WIECHOWSKI A. Effect of flux additions on the kinetics of chromite ore reduction with carbon [C]//INFACON 7. Trondheim, Norway: FFF, 1995: 371−382.

[11] WEBER P, ERIC R H. The reduction of chromite in the presence of silica flux [J]. Minerals Engineering, 2006, 19: 318−324.

[12] LEKATOU A, WALKER R D. Effect of SiO_2 addition on solid state reduction of chromite concentrate [J]. Ironmaking & Steelmaking, 1997, 24: 133−143.

[13] DUONG H V, JOHNSTON R F. Kinetics of solid state silica fluxed reduction of chromite with coal [J]. Ironmaking & Steelmaking, 2000, 27: 202−206.

[14] URQUHART R C, JOCHENS P R, HOWAT D D. A laboratory investigation of the smelting mechanisms associated with the production of high-carbon ferrochromium [C]//Proceedings INFACON 1974. South Africa, Johannesburg, 1974: 231−245.

[15] WEBER P, ERIC R H. Solid-state fluxed reduction of LG-6 chromite from the Bushveld complex [C]//INFACON 6. Proceeding of the 6th International Ferroalloys Congress. South Africa, Cape Town, 1992: 71−77.

[16] DING Y L, WARNER N A. Catalytic reduction of carbon-chromite composite pellets by lime [J]. Thermochimica Acta, 1997, 292: 85−94.

[17] NEIZEL B W, BEUKES J P, VAN ZYL P G, DAWSON N F. Why is $CaCO_3$ not used as an additive in the pelletised chromite pre-reduction process? [J]. Minerals Engineering, 2013, 45: 115−120.

[18] KATAYAMA H G, TOKUDA M, OHTANI M. Promotion of the carbothermic reduction of chromite ore by the addition of borates [J]. The Iron and Steel Institute of Japan, 1986, 72: 1513−1520.

[19] SOKHANVARAN S, PAKTUNC D. The effect of fluxing agent on direct reduction of chromite ore [C]//Conference of Metallurgists. Vancouver. Canada: Metallurgy and Materials Society, 2017: 9696.

[20] YU D, PAKTUNC D. Direct production of ferrochrome by segregation reduction of chromite in the presence of calcium chloride [J]. Metals, 2018, 8: 69.

[21] YU D, PAKTUNC D. Calcium chloride-assisted segregation reduction of chromite: Influence of reductant type and the mechanism [J]. Minerals, 2018, 8: 45.

[22] HOLYWELL G, BREAULT R. An overview of useful methods to treat, recover, or recycle spent potlining [J]. JOM, 2013, 65: 1441−1451.

[23] PAWLEK R P. Spent potlining: Water soluble components, landfill and alternative solutions [C]//Light Metals 1993. Pittsburgh, PA: The Minerals, Metals & Materials Society, 1993: 399−405.

[24] PAWLEK R P. Spent potlining: An update [C]//Light Metals 2012. Springer, Cham, 2012: 1313−1317.

[25] PONG T K, ADRIEN R J, BESIDA J, O'DONNELL T A, WOOD D G. Spent potlining—A hazardous waste made safe [J]. Process Safety and Environmental Protection, 2000, 78: 204−208.

[26] NIKITIN L D, et al. Use of aluminium production wastes in the charge of blash furnace at the west Siberian metallurgical plant [J]. Ferrous Metallurgy, Bulletin of Scientific, Technical and Economic Information, 2001, 11: 33−36. (in Russian)

[27] von KRÜGER Paulo. Use of spent potlining (SPL) in ferro silico manganese smelting [C]//Light Metals 2011. Hobokem, NJ, USA: John Wiley & Sons, Inc., 2011: 275−280.
[28] YU D, CHATTOPADHYAY K. Numerical simulation of copper recovery from converter slags by the utilisation of spent potlining (SPL) from aluminium electrolytic cells [J]. Canadian Metallurgical Quarterly, 2016, 55: 251−260.
[29] YU D, CHATTOPADHYAY K. Fluxing molten converter slags with spent potlining (SPL) for metal recovery [C]//COM 2015. Toronto, Canada: Canadian Institute of Mining, Metallurgy and Petroleum, 2015: 1−11.
[30] AUGOOD D R, SCHLAGER R J. Potlining flux in making steel [C]//Light Metals 1983. Pittsburgh, PA: The Minerals, Metals & Materials Society, 1983: 1037−1043.
[31] GAO L, MOSTAGHEL S, RAY S, CHATTOPADHYAY K. Use of SPL (spent pot-lining) as as alternative fuel in metallurgical furnaces [J]. Metallurgical and Materials Transactions E, 2016, 3: 179−188.
[32] GOMES V, DRUMOND P Z, NETO J O P, LIRA A R. Co-processing at cement plant of spent potlining from aluminium industry [C]//Essential Readings in Light Metals. Springer, Cham, 2005: 507−513.
[33] FROST I C. An elutriating tube for the specific gravity separation of minerals [J]. The American Mineralogist, 1959, 44: 886−890.
[34] SCHNEIDER A C, RASBAND W S, ELICEIRI K W. NIH Image to ImageJ: 25 years of image analysis [J]. Nature Methods, 2012, 9: 671−675.
[35] BALE C W, BELISLE E, CHARTRAND P, DECTEROV S A, ERIKSSON G, GHERIBI A E, HACK K, JUNG I H, KANG Y B, MELANCON J, PELTON A D, PETERSEN S, BOBELIN C, SANGSTER J, van ENDE M-A. FactSage thermochemical software and databases, 2010−2016 [J]. Calphad, 2016, 54: 35−53.
[36] ROSCOE R. The viscosity of suspensions of rigid spheres [J]. British Journal of Applied Physics, 1952, 3: 267−269.
[37] SATO Hiroaki. Viscosity measurement of subliquidus magmas: 1707 basalt of Fuji volcano [J]. Journal of Mineralogical and Petrological Sciences, 2005, 100: 133−142.
[38] MARSH B D. On the crystallinity, probability of occurrence, and rhyology of lava and magma [J]. Contributions to Mineralogy and Petrology, 1981, 78: 85−98.
[39] LIU S, ZHOU Y, XING X, WANG J, REN X, YANG Q. Growth characteristics of primary M7C3 carbide in hypereutectic Fe−Cr−C alloy [J]. Scientific Reports, 2016, 6: 32941.
[40] LEŠKO A, NAVARA E. Microstructural characterization of high-carbon ferrochrome [J]. Materials Characterization, 1996, 36: 349−356.
[41] HU X, TENG L, WANG H, ÖKVIST L S, YANG Q, BJÖRKMAN B, SEETHARAMAN S. Carbothermic reduction of synthetic chromite with/without the addition of iron powder [J]. ISIJ International, 2016, 56: 2147−2155.
[42] van STADEN Y, BEUKES J P, VAN ZYL P G, RINGDALEN E, TANGSTAD M, KLEYNHANS E L J, BUNT J R. Dam-ring formation in chromite pre-reduction rotary kilns — Influence of pulverised carbonaceous fuel and ore composition [C]//Infacon XV: International Ferro-Alloys Congress. Cape Town, South Africa: Southern African Institute of Mining and Metallurgy, 2018: 25−28.

利用铝电解槽废旧阴极碳热还原铬铁矿

于大伟[1,2], Dogan PAKTUNC[1]

1. CanmetMINING, Natural Resources Canada 555 Booth Street, Ottawa, Ontario K1A 0G1, Canada;
2. 中南大学 冶金与环境学院，长沙 410083

摘　要：铝电解槽废旧阴极(SPL)是铝电解生产过程中产生的废料，被用作造渣熔剂与碳源来碳热还原铬铁矿。本研究的主要目标是促进碳热还原过程中铬铁合金颗粒的生长，以利于后续过程中合金与渣相的分离。实验证明相对于采用石墨作为还原剂，SPL 中的碳组分能够更有效地还原铬铁矿。铬铁矿还原过程中矿物颗粒表面形成惰性的尖晶石层($MgAl_2O_4$)，从而阻碍反应的进行以及铬铁合金的生长。SPL 中的造渣组分(例如霞石及 NaF)在较低温度下(约 1300 °C)形成熔渣，并部分熔解尖晶石以及铬铁矿相。通过破坏铬铁矿颗粒表面的惰性尖晶石层、促进传质过程以及提高还原温度(例如 1500 °C)实现铬铁合金颗粒的生长。在还原温度为 1500 °C 以及采用 SPL 作为添加剂条件下，还原得到较为粗大的铬铁合金颗粒，采用淘析法能够实现合金与渣相的有效分离。

关键词：铬铁矿；碳热还原；铬铁合金；铝电解槽废旧阴极

(Edited by Xiang-qun LI)